electronics

MDPI

Article

A Minimally Invasive Approach for Precise Demagnetization Fault Diagnosis in Permanent Magnet Synchronous Motors Under Arbitrary Demagnetization Patterns

Caixia Gao [1], Zhe Song [1], Jianjun Dang [1,*], Xiaozhuo Xu [1] and Jikai Si [2]

[1] School of Electrical Engineering and Automation, Henan Polytechnic University, Jiaozuo 454150, China; gcx@hpu.edu.cn (C.G.); 13007521365@163.com (Z.S.); xxz@hpu.edu.cn (X.X.)
[2] College of Electrical Engineering, Zhengzhou University, Zhengzhou 454001, China; sijikai@zzu.edu.cn
* Correspondence: dangjianjun@hpu.edu.cn

Abstract

Accurate demagnetization fault diagnosis is critical to ensuring the safety and reliability of permanent magnet synchronous motors (PMSMs). However, the number, location, and severity of demagnetized permanent magnets are mutually coupled, leading to a combinatorial explosion of fault patterns. Existing methods are largely limited to idealized assumptions involving single-magnet demagnetization or uniform demagnetization of multiple magnets, making it difficult to characterize the random nature of demagnetization in practical operation. Thus, this paper proposes a precise demagnetization fault diagnosis method based on a novel search coil (SC) configuration, in which only two toroidal-yoke-type search coils are installed in the stator slots. The proposed method partitions the rotor permanent magnets into several modules and categorizes the infinite demagnetization fault patterns into 26 representative patterns, effectively addressing the issue of fault mode explosion. Theoretical analysis and experimental results show that the voltage waveforms of the search coil over a single electrical period exhibit significant and stable differences across the identified patterns. By constructing feature vectors based on these differences, a physically interpretable mapping between the feature vectors and fault patterns is established. Combined with a corresponding pattern recognition algorithm, the proposed method enables fast and accurate differentiation of the 26 patterns without the need for complex machine learning models, thereby achieving precise localization of demagnetized permanent magnets. Simulation and experimental results verify the correctness and effectiveness of the proposed method.

Keywords: demagnetization fault localization; different severities of demagnetization; PM synchronous motor; residual voltage; search coil

Check for updates

Academic Editor: Marcin Witczak

Received: 2 April 2026
Revised: 7 May 2026
Accepted: 11 May 2026
Published: 14 May 2026

Copyright: © 2026 by the authors. Licensee MDPI, Basel, Switzerland. This article is an open access article distributed under the terms and conditions of the Creative Commons Attribution (CC BY) license.

1. Introduction

Permanent magnet synchronous motors (PMSMs) with high power density and high torque-to-volume ratios have been widely used in different applications such as electric vehicles, aerospace, and other industrial areas [1,2]. However, due to the harsh working environment and frequent load changes, PMSMs may induce irreversible demagnetization faults (DFs), resulting in motor performance degradation and system reliability degradation [3–5]. Therefore, an efficient and accurate method of fault detection and fault location can provide important information for regular motor maintenance and fault tolerance compensation.

A demagnetization fault reduces the air-gap flux, which causes changes in different motor signals, including current, voltage, vibration, magnetic flux, and other signals. Since the current signal is easy to acquire and does not need extra sensors, the method based on motor current signature analysis (MCSA) is among the online diagnosis methods that receives the most attention [6–8]. This method is non-invasive and mainly focuses on spectral analysis of the stator currents, searching for certain harmonic components caused by faults. Some advanced signal processing technologies need to be used for spectral or time–frequency analysis, such as the fast Fourier transform (FFT) [6], the continuous wavelet transform (CWT), or the discrete wavelet transform (DWT) [7], and so on. In recent years, automatic diagnostic techniques incorporating current signal analysis have developed rapidly as machine learning (ML) techniques mature. Ref. [8] uses wavelet packet transform (WPT) and a 1-D convolution neural network (1D-CNN) to extract fault features from the current signature. Ref. [9] detects and classifies stator winding turn-to-turn short-circuit faults and permanent magnet demagnetization faults using FFT and shallow neural networks. However, the same fault characteristics can be caused by different faults, and the fault harmonic components are not present in uniform demagnetization faults, which affects the accuracy of fault diagnosis. In addition, the current harmonics are easily influenced by the inverter and controller regulator. Therefore, methods based on the zero-sequence voltage component (ZSVC) [10,11] are proposed; these calculate the voltage difference between the neutral point of the stator winding and the artificial neutral point. Thus, the disadvantage of this method is that you must have the ability to access the neutral point of the machine.

Demagnetization faults can disrupt air-gap flux, resulting in unbalanced torque and motor vibration. Therefore, Ref. [12] introduces an efficient method using torque spectra calculation to diagnose demagnetization faults in surface-mounted permanent magnet synchronous motors (SMPMSMs). In [13,14], fault diagnosis methods based on vibration signal analysis for PMSMs are proposed. However, the raw signals of torque or vibration have a high level of noise in them that can interfere with fault diagnosis. Therefore, some scholars have chosen to use the flux signal, which directly reflects the condition of the magnet, as the fault diagnosis signal. In [15,16], the leakage flux around the PMSM is acquired using a sensor and used for diagnostics. However, the magnetic leakage signal is weak, which makes fault detection and location more difficult. In order to obtain more obvious fault characteristics, Ref. [17] uses a sensor to obtain the three-line air-gap magnetic flux density signal for off-line diagnosis of demagnetization faults in double-sided permanent magnet synchronous linear motors (DPMLSMs). In [18], a magnetic induction device mounted inside the motor is designed and applied to complete the health diagnosis of PMs by monitoring the air-gap flux density. However, the use of expensive sensors to obtain the signals would increase diagnostic costs. Considering that fault-induced changes in air-gap flux can be reflected in the voltage of the search coil (SC), SC-based methods have received a great deal of attention in recent years. Although the methods based on SCs are invasive, they are favored for their low cost and efficiency. In [18], the fundamental frequency components of the voltages generated by 12 search coils winding around the stator teeth are utilized for health monitoring and multi-fault detection in PMSMs. Furthermore, the direction of eccentricity and the location of winding shorted turns can be found. Based on the hardware described in [19], a specific diagnosis method is proposed to identify the fault parameters in [20]. However, it causes high invasiveness when search coils are installed around all the stator teeth. To reduce the invasiveness of the search coil (SC) scheme, researchers have explored two major technical paths: One is to optimize the installation form of the search coil, and the other is to reduce the number of required search coils. In terms of optimizing the installation form, reference [21] developed

a planar search coil (PSC) made of a flexible printed circuit board (FPCB). This PSC is only 0.1 mm thick and can be directly attached to the surface of the stator teeth, without having to go around the tooth tips or occupy the limited slot space of the stator, thereby significantly reducing the structural invasiveness and installation difficulty of the traditional wound-type SC. On the other hand, in the technical path of reducing the number of search coils, Ref. [22] proposed using a single air-gap flux search coil to detect and classify various faults such as uniform and local demagnetization, dynamic eccentricity, and load imbalance. To accurately locate the faulty PMs, a novel method using three toroidal-yoke search coils is proposed in [23]. To further reduce its invasiveness and algorithm complexity, Ref. [24] uses two toroidal-yoke search coils connecting in forward series to locate faulty PMs. The two methods described above significantly reduce the invasiveness of the SC and the complexity of the diagnostic algorithm, and they can also accurately locate faulty PMs.

However, both of these methods reduce the number of search coils by simplifying the fault model, specifically by assuming that all demagnetized PMs exhibit identical demagnetization severity. This assumption fundamentally deviates from the inherent randomness and non-uniformity of real-world demagnetization faults. Consequently, they are limited to single-PM demagnetization or multi-PM demagnetization with uniform severity and cannot distinguish the relative demagnetization levels among the PMs. In contrast, the proposed method retains a low sensor count without resorting to such simplifications. This is enabled by the 26-pattern framework, which reduces arbitrary fault cases to a finite, distinguishable set, thereby achieving precise fault localization without the uniform demagnetization assumption. In addition, the interference from time-varying load conditions in fault diagnosis signals is an important engineering challenge that limits the practical application of the method. In actual PMSM systems, they often operate under non-steady-state load conditions. Load fluctuations can alter the amplitude of the stator current and shift the degree of magnetic saturation, thereby modulating the fault characteristic signal components and significantly increasing the difficulty of extracting effective fault features. Ref. [25] points out that load changes introduce strong coupling effects and emphasizes the importance of suppressing load-coupling interference to accurately extract fault features. Ref. [26] developed a parameter-free mechanical parameter identification method and completed experimental verification under time-varying load conditions, fully demonstrating that actual PMSM drive systems should have the ability to cope with various non-steady-state operating conditions. In response to the above issues, this paper proposes a demagnetization localization method for PMSM based on the residual voltage of SC, which applies to locating demagnetized faults with different fault severities of demagnetization.

The rest of the paper is organized as follows. Section 2 introduces the arrangement of the SC and the acquisition method of the induced voltage signal. Meanwhile, the mathematical model of the residual voltage of SC generated by a single faulty PM is established, and the residual voltages generated by different locations of faulty PMs are investigated by the model. Section 3 selects two fault localization indicators through a detailed study of the residual voltage waveform characteristics of 26 fault modes and proposes a demagnetization fault localization method. In Section 4, simulations and experiments are conducted to verify the effectiveness of the method. Section 5 concludes the work.

2. Mathematical Modeling of Demagnetization Fault Diagnosis Signals

2.1. Search Coil Working Mechanism

The magnetomotive force (MMF) produced by a PM can be expressed as:

$$F_{PM} = H_m h_m \tag{1}$$

where F_{PM} is the MMF, and H_m and h_m represent the PM coercivity and thickness, respectively.

When a PM undergoes irreversible demagnetization, its coercivity decreases. This reduces the MMF F_{PM} as defined in Equation (1), thereby weakening the magnetic field it produces. The resulting change in the magnetic field can be detected by installing search coils (SCs) on the motor stator. According to Faraday's induction law, this variation in the magnetic field induces a corresponding voltage change in the SC, as given by Equation (2):

$$e_{sc} = -N_{sc}\frac{d\phi_{sc}}{dt} \tag{2}$$

where e_{sc} is the induced voltage of the SC, N_{sc} is the number of turns of the SC, and Φ_{SC} is the PM flux linked to the SC.

Consequently, the residual voltage of the SC serves as an ideal diagnostic signal for demagnetization faults. It is defined as the difference between the measured voltage signal and the voltage signal under healthy motor conditions. Studies [23,24] have demonstrated that the SC residual voltage exhibits an approximately linear relationship with the demagnetization severity of each individual PM. Therefore, the residual voltage of the SC can be obtained from the linear superposition of the residual voltages generated by each individual PM, which corresponds to the linearized formulation of Faraday's induction law.

$$e_{jre} = \sum_{i}^{2p} e_{jrei} = \sum_{i}^{2p} e_{jhi} - e_{jfi} = -N_{sc}\frac{d}{dt}\left(\sum_{i}^{2p} D_i \phi_{jhi}\right) \tag{3}$$

where p is the number of pole pairs; e_{jre} and e_{jrei} denote the induced residual voltage of the j-th SC (SC_j) due to all rotor PMs and the i-th PM (PM_i), respectively; e_{jhi} and e_{jfi} are the induced voltages of the SC_j under the healthy and demagnetized conditions of PM_i, respectively; and Φ_{jhi} is the healthy PM_i flux linked to the SC_j. The demagnetization coefficient D_i for PM_i, which quantifies as demagnetization severity, is defined by Equation (4):

$$D_i = \frac{F_{PMi-h} - F_{PMi-d}}{F_{PMi-h}} \times 100\% \tag{4}$$

where $F_{PMi\text{-}h}$ and $F_{PMi\text{-}d}$ represent the MMF for the healthy and demagnetized conditions of PM_i, respectively. The coefficient D_i ranges from 0 to 1, corresponding to the fully healthy and the completely demagnetized states.

To obtain the positional information of the demagnetized magnet, two identical toroidal yoke coils are installed in the stator slots and connected in positive series to form a search coil, as shown in Figure 1. Each toroidal-yoke coil is placed in the inner and outer stator slots in the PMSM. Spacing the two yoke coils approximately one pole pitch apart enhances the signal amplitude, thus improving the SNR. This hardware configuration is generally applicable to any slotted-stator PMSM, as the toroidal-yoke coils are wound around the stator yoke through the slot region without interfering with the main winding or the air gap. The operating mechanism of the novel searching coil will be analyzed in the following section.

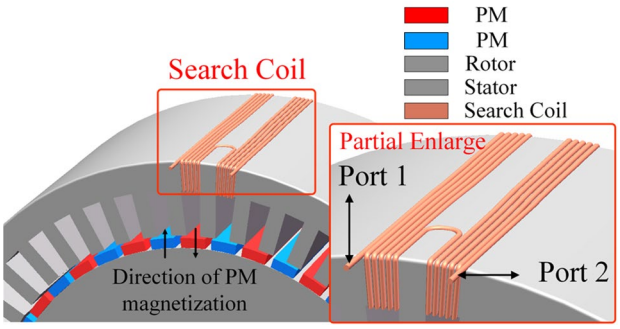


Figure 1. Search coil arrangement.

2.2. Mathematical Model of SC Residual Voltage

A mathematical model of the SC residual voltage generated by a single demagnetized PM is established according to [23], which can be expressed in the Fourier series as:

$$E_{re-i} = \begin{cases} \sum_{n=-\infty}^{n=+\infty} (-1)^{i-1} D_i[E_n \sin(n\alpha - n(i-1)\pi)] & (i-1)\pi \le \alpha \le (i-1)\pi + \theta_{cp} \\ \sum_{n=-\infty}^{n=+\infty} (-1)^{i-1} D_i[E_n \sin(n\alpha - n(i-1)\pi) + E_n \sin(n\alpha - n(i-1)\pi - \theta_{cp})] & (i-1)\pi + \theta_{cp} \le \alpha \le i\pi \\ \sum_{n=-\infty}^{n=+\infty} (-1)^{i-1} D_i[E_n \sin(n\alpha - n(i-1)\pi - \theta_{cp})] & i\pi \le \alpha \le i\pi + \theta_{cp} \\ 0 & others \end{cases} \quad (5)$$

where $E_{re\text{-}i}$ is the SC residual voltage induced by PM_i. E_n is the amplitude of the nth component of $E_{re\text{-}i}$, α is the electrical angle from the coordinate origin, which is located at the geometric center line of PM_1 and PM_{2p}, and θ_{cp} is the motor slot pitch.

For the sake of simplicity, the fundamental component of E_n is only considered, and E_{PMi} can be simplified as Equation (6):

$$E_{re-i} = \begin{cases} (-1)^{i-1} D_i[E_1 \sin(\alpha - (i-1)\pi)] & (i-1)\pi \le \alpha \le (i-1)\pi + \theta_{cp} \\ (-1)^{i-1} D_i[E_1 \sin(\alpha - (i-1)\pi) + E_1 \sin(\alpha - (i-1)\pi - \theta_{cp})] & (i-1)\pi + \theta_{cp} \le \alpha \le i\pi \\ (-1)^{i-1} D_i[E_1 \sin(\alpha - (i-1)\pi - \theta_{cp})] & i\pi \le \alpha \le i\pi + \theta_{cp} \\ 0 & others \end{cases} \quad (6)$$

The normalization process is carried out to eliminate the effects of the variations in the motor speed and load on the fundamental component.

$$E_{n-i} = \frac{E_{re-i}}{\max(|E_{re-i}|)} \quad (7)$$

Using Equations (5)–(7), the residual voltage waveforms generated by different demagnetized PMs are analyzed.

As shown in Figure 2, $E_{n\text{-}i}$ is located in the interval $[(i-1)\pi, i\pi + \theta_{cp}]$ when PM_i is demagnetized. $E_{n\text{-}(i+1)}$ is located in the interval $[i\pi, (i+1\pi)\pi + \theta_{cp}]$ when PM_{i+1} is demagnetized. $E_{n\text{-}(i-1)}$ is located in the interval $[(i-2)\pi, (i-1\pi) + \theta_{cp}]$ when PM_{i-1} is demagnetized. Thus, the residual voltage located in the interval $[(k-1)\pi, (k+1)\pi]$ can be calculated using Equation (8).

$$E_k = \begin{cases} E_{PM2p} + \sum_{i=1}^{2} E_{PMi}(k=1) \\ \sum_{i=2k-2}^{2k} E_{PMi}(k=2,3,4\cdots p) \end{cases} \quad (8)$$

where E_k is the residual voltage of kth electrical period. k is the electrical period number.

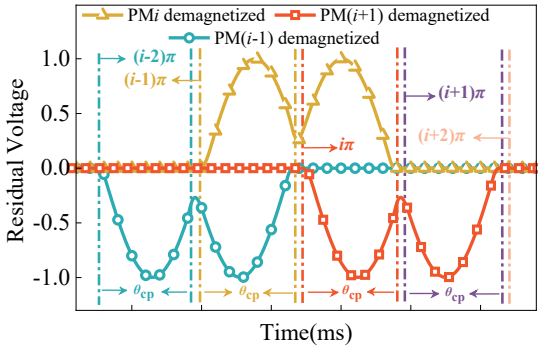


Figure 2. The $E_{n\text{-}i}$ generated by different demagnetized PMs.

Equation (8) implies that the SC signal in the k-th electrical period is determined by the states (healthy or faulty) of the three PMs in the k-th module(PM($2k-2$), PM($2k-1$), and PM($2k$)). Each of the three permanent magnets can be either healthy or demagnetized, giving rise to eight state combinations, as shown in Table 1.

Table 1. Eight states combination of three consecutive PMs.

State Code	The PM Number That Determines the Waveform of the Residual Voltage's kth Electrical Period					
	PM_{2p}	PM_1	PM_2	PM_{2k-2}	PM_{2k-1}	PM_{2k}
S0 (000)	0	0	0	0	0	0
S1 (100)	1	0	0	1	0	0
S2 (010)	0	1	0	0	1	0
S3 (001)	0	0	1	0	0	1
S4 (101)	0	1	1	0	1	1
S5 (110)	1	1	0	1	1	0
S6 (101)	1	0	1	1	0	1
S7 (111)	1	1	1	1	1	1

In Table 1, "0" indicates that the PM is healthy, and "1" indicates that the PM has demagnetized. Taking S4 (101) as an example, this state code signifies that the PM_{2p} is healthy, whereas PM_1 and PM_2 are demagnetized, resulting in a residual signal appearing in the first electrical period ($k = 1$). Similarly, if E_{PMi} is located in the kth electrical period ($1 < k \leq p$), S4 indicates that PM_{2k-2} is healthy, and PM_{2k-1} and PM_{2k} are faulty.

3. Eight State Combinations of Three Consecutive PMs

3.1. Fault Modes Analysis

When a demagnetization fault occurs in a multi-pole motor, different combinations of the number, location, and severity of demagnetization PMs can produce a large number of fault modes. To address these issues, the rotor permanent magnets are partitioned into p modules. Each module contains three PMs, resulting in eight state combinations. According to the relative demagnetization severities among the magnets within a module, the infinite demagnetization patterns are transformed into 26 representative patterns (as listed in Table 2, which takes the first module as an example) for identification, fundamentally overcoming the combinatorial explosion problem.

Table 2. Twenty-six fault modes occurring in the first electrical period.

State Code	Fault Mode		Fault PMs (Demagnetization Degree)
S0 (000)	F0		None
S1 (100)	F1		$\delta 2p$ (0.5)
S2 (010)	F2		$\delta 1$ (0.5)
S3 (001)	F3		$\delta 2$ (0.5)
S4 (101)	F4		$\delta 2p$ (0.3) < $\delta 2$ (0.5)
	F5		$\delta 2p = \delta 2 = 0.5$
	F6		$\delta 2p$ (0.5) > $\delta 2$ (0.3)
S5 (011)	F7		$\delta 1$ (0.3) < $\delta 2$ (0.5)
	F8		$\delta 1 = \delta 2 = 0.5$
	F9		$\delta 1$ (0.5) > $\delta 2$ (0.3)
S6 (110)	F10		$\delta 2p$ (0.3) < $\delta 1$ (0.5)
	F11		$\delta 2p = \delta 1 = 0.5$
	F12		$\delta 2p$ (0.5) > $\delta 1$ (0.3)
S7 (111)	S7 (a) $\delta 2p = \delta 2$	F13	$\delta 2p$ (0.5) = $\delta 2$ (0.5) < $\delta 1$ (0.7)
		F14	$\delta 2p = \delta 1 = \delta 2 = 0.7$
		F15	$\delta 1$ (0.3) < $\delta 2p$ (0.5) = $\delta 2$ (0.5)
	S7 (b) $\delta 2p < \delta 2$	F16	$\delta 1$ (0.15) < $\delta 2p$ (0.3) < $\delta 2$ (0.7)
		F17	$\delta 1$ (0.3) = $\delta 2p$ (0.3) < $\delta 2$ (0.7)
		F18	$\delta 2p$ (0.3) < $\delta 1$ (0.5) < $\delta 2$ (0.7)
		F19	$\delta 2p$ (0.3) < $\delta 1$ (0.7) = $\delta 2$ (0.7)
		F20	$\delta 2p$ (0.3) < $\delta 2$ (0.7) < $\delta 1$ (0.9)
	S7 (c) $\delta 2p > \delta 2$	F21	$\delta 2p$ (0.7) > $\delta 2$ (0.3) > $\delta 1$ (0.15)
		F22	$\delta 2p$ (0.7) > $\delta 2$ (0.3) = $\delta 1$ (0.3)
		F23	$\delta 2p$ (0.7) > $\delta 1$ (0.5) > $\delta 2$ (0.3)
		F24	$\delta 2p$ (0.7) = $\delta 1$ (0.7) > $\delta 2$ (0.3)
		F25	$\delta 1$ (0.9) > $\delta 2p$ (0.7) > $\delta 2$ (0.3)

By analyzing the SC signal over one mechanical period, the states of the permanent magnets in each module can be diagnosed sequentially. Specifically, the signal within each electrical period is evaluated to determine which of the eight fault patterns corresponds to that module, thereby enabling precise demagnetization fault localization. In this section, the diagnostic signals under the 26 demagnetization fault patterns are analyzed to extract feature vectors that can distinguish the eight fault states, and their robustness is evaluated. Note that different patterns within the same fault state need not be further distinguished, provided that their waveforms differ significantly from those of other fault modes.

As shown in Table 2, S0 denotes that all three PMs in the module are healthy. S1–S3 denote that only one of the three PMs is demagnetized, and one fault mode is listed for each state code, which is represented by F1, F2, and F3, respectively. S4–S6 denote that there are two faulty PMs in the module. Depending on the correlation of the severities of demagnetization of the two faulty PMs, three fault modes are listed for each state code, which are represented by F4–F6, F7–F9, and F10–F12. S7 denotes that three PMs are all demagnetized and breaks it down into three scenarios: $\delta 2p = \delta 2$ (S7(a)), $\delta 2p < \delta 2$ (S7(b)), and $\delta 2p > \delta 2$ (S7(c)). Then, three fault modes are listed in S7(a) and represented by F13–F15, five fault modes are listed in S7(b) and represented by F16–F20, and five fault modes are listed in S7(c) and represented by F21–F25. Therefore, there are a total of 13 fault modes in S7.

3.2. Demagnetization Fault Diagnosis Indicators Selection

Based on the 26 fault modes listed in Table 2, the normalized residual voltage of the SC under preset demagnetization severities is analyzed using the proposed mathematical model.

As shown in Figure 3, the normalized residual voltage waveform is divided into two half-cycles by the midline of the electrical period. A comparative analysis of the residual voltage signals under the 26 demagnetization fault modes reveals that the waveforms corresponding to the eight fault states are distinguishable. Based on this, four feature vectors, consisting of the defined signal average value ($V_{d\text{-}av}$) in the first and second half-cycles and the zero-crossing point number (Z_C) of the waveform, are extracted to effectively distinguish the eight fault states and achieve precise localization of the demagnetization fault.

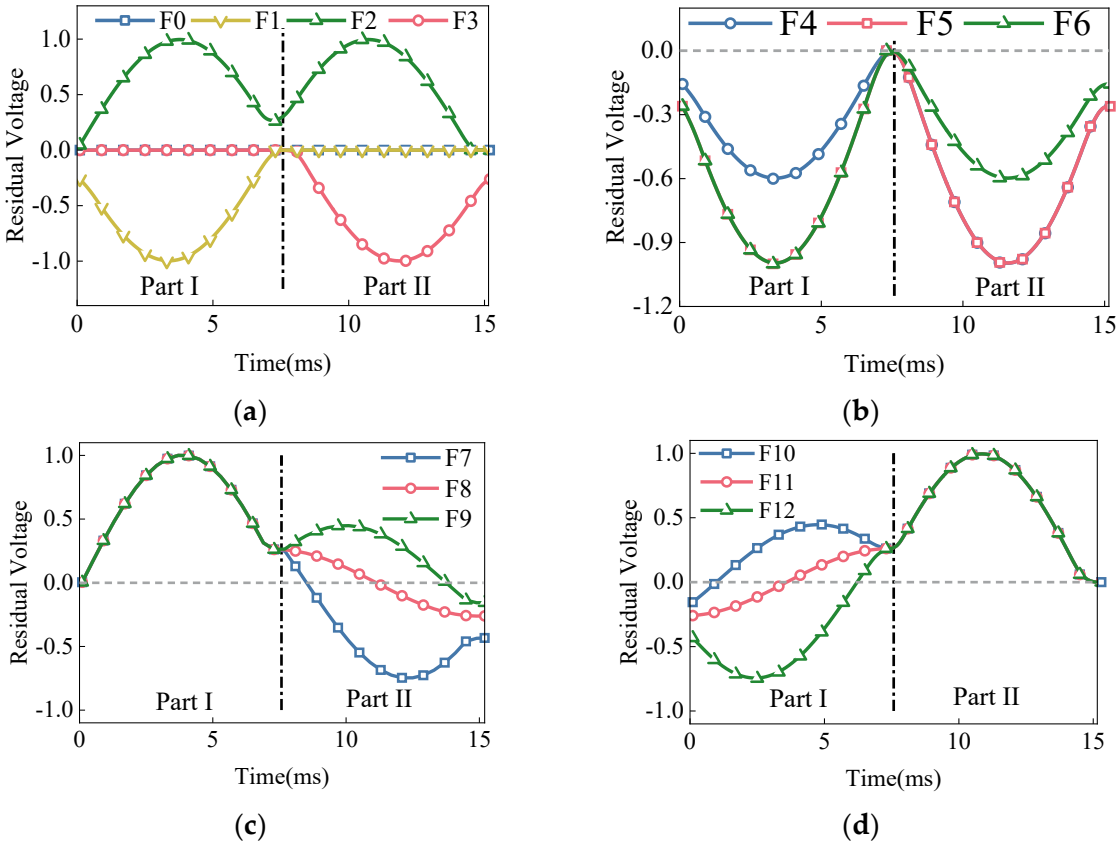


Figure 3. The normalized residual voltage waveforms in S0–S6. (**a**) S0–S3; (**b**) S4; (**c**) S5; (**d**) S6.

(1) The defined signal average value ($V_{d\text{-}av}$): First, the signal average value (V_{av}) of each part is calculated by Equation (9). Then, $V_{d\text{-}av}$ is defined as 1 when V_{av} is more than the threshold value (V_{thre}); $V_{d\text{-}av}$ is defined as -1 when V_{av} is less than $-V_{thre}$; $V_{d\text{-}av}$ is defined as 0 when V_{av} is between $-V_{thre}$ and V_{thre}.

$$\begin{cases} V_{av} = \dfrac{2\sum_{k=1}^{N} V_k}{N} \\ N = \dfrac{f_s}{f_e} \end{cases} \tag{9}$$

where V_{av} is the signal average value, and V_k is the sampling residual voltage. N is the number of sampling points for the residual voltage. f_s is the sampling frequency, and f_e is the electrical frequency of the motor.

For motors with different rated powers and pole–slot combinations, first, obtain the average value of the normalized residual voltage of the detection coil for each half electrical cycle under healthy conditions and across different speeds and loads, and take the maximum absolute value among them as the health state reference. Then, multiply this base value by a safety factor λ greater than 1 to obtain the final diagnostic threshold, thereby fully considering the influence of factors such as the noise environment. In practical applications, the coefficient λ should be flexibly determined based on the operating conditions of the motor application field and the performance requirements of the diagnostic system. Therefore, the calculation of the threshold is as shown in Equation (10):

$$V_{\text{thre}} = \lambda \times V_{\text{h-av-max}} \tag{10}$$

where λ is the safety factor, and $V_{\text{h-max}}$ is the maximum average value of the normalized residual voltage in the search coil over each half-cycle during normal motor operation.

(2) The zero-crossing point number (Z_C): As shown in Figure 4, A and B are two data points with one positive and one negative, the nth and $(n + 1)^{th}$ data points, respectively. Thus, there is one zero point between A and B, meaning there exists a zero-crossing point. If Z_C is 1, it means that there is a zero-crossing point in the corresponding part, and 0 means that there is no zero-crossing point in the corresponding part.

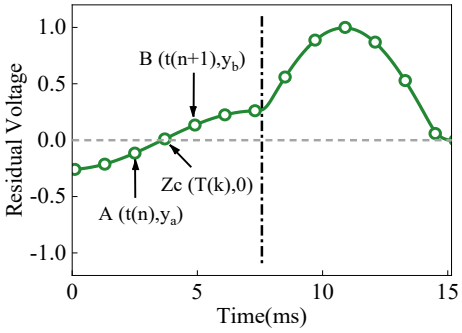


Figure 4. The zero-crossing point.

Table 3 shows the relationship between the four fault diagnosis feature vectors and state combinations.

Table 3. The relationship between fault localization indicators and state combinations of S0–S7.

State Combination	Fault Mode	Part I		Part II	
		Z_C	$V_{d\text{-}av}$	Z_C	$V_{d\text{-}av}$
S0 (000)	F0	0	0	0	0
S1 (100)	F1	0	−1	0	0
S2 (010)	F2	0	1	0	1
S3 (001)	F3	0	0	0	−1
S4 (101)	F4	0	−1	0	−1
	F5	0	−1	0	−1
	F6	0	−1	0	−1
S5 (011)	F7	0	1	1	−1
	F8	0	1	1	0
	F9	0	1	1	1
S6 (110)	F10	1	1	0	1
	F11	1	0	0	1
	F12	1	−1	0	1

Table 3. *Cont.*

State Combination	Fault Mode	Part I		Part II	
		Z_C	$V_{d\text{-}av}$	Z_C	$V_{d\text{-}av}$
S7 (111)	F13	1	1	1	1
	F14	1	0	1	0
	F15	1	−1	1	−1
	F16	1	−1	1	−1
	F17	1	0	1	−1
	F18	1	1	1	−1
	F19	1	1	1	0
	F20	1	1	1	1
	F21	1	−1	1	−1
	F22	1	−1	1	0
	F23	1	−1	1	1
	F24	1	0	1	1
	F25	1	1	1	1

As we can see in Table 3 and Figure 5, the fault diagnosis feature vectors in S0 to S7 are different from each other. Therefore, S0 to S7 can be classified by four fault diagnosis feature vectors.

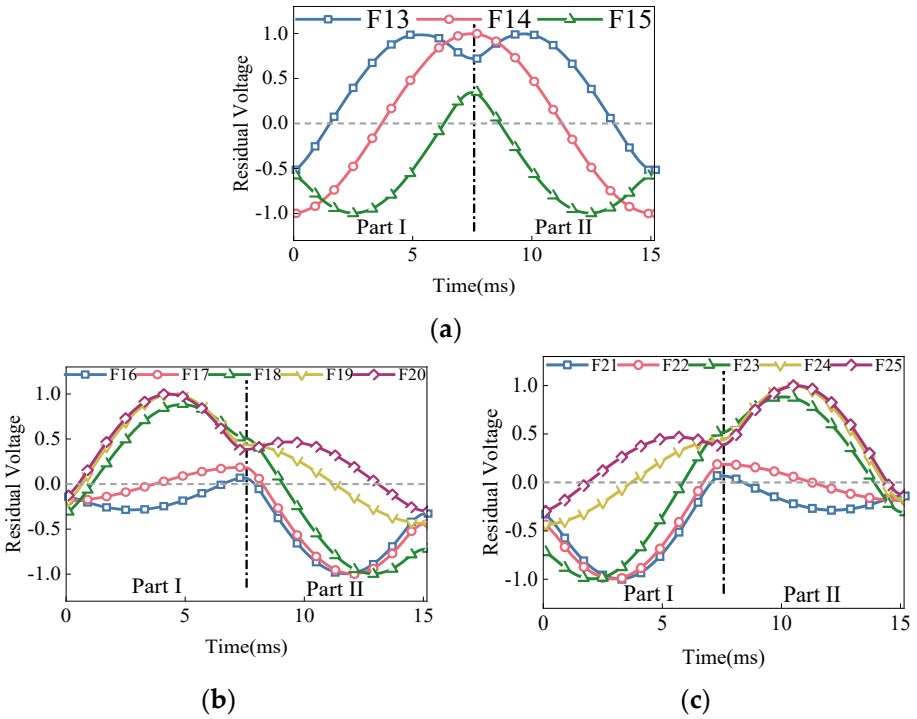


Figure 5. The normalized residual voltage waveforms in S7.(**a**) F13–F15; (**b**) F16–F20; (**c**) F21–F25.

3.3. Demagnetization Fault Diagnosis Indicators Analysis

The results in Section 3.2 are obtained based on a predetermined demagnetization severity. This section analyzes the demagnetization faults under different demagnetization severities. For S5, for example, the different demagnetization severities are listed in Table 4, and the normalized residual voltage waveforms are shown in Figure 6.

Table 4. Different fault severities of demagnetized PMs in S5.

Fault Mode	Fault Degree
F7 $\delta1 < \delta2$	$\delta1 = 0.5, \delta2 = 0.7$ $\delta1 = 0.5, \delta2 = 0.9$ $\delta1 = 0.5, \delta2 = 1.0$ $\delta1 = 0.3, \delta2 = 1.0$
F8 $\delta1 = \delta2$	$\delta1 = 0.5, \delta2 = 0.5$
F9 $\delta1 > \delta2$	$\delta1 = 0.5, \delta2 = 0.15$ $\delta1 = 0.5, \delta2 = 0.3$

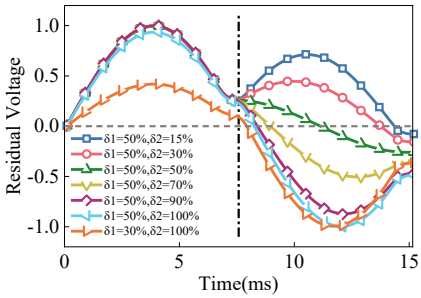


Figure 6. The normalized residual voltage waveforms under different demagnetization severities of PMs in S5.

As shown in Figure 6, when PM_1 and PM_2 are demagnetized, there is a zero-crossing point in Part II which moves to the electrical cycle midline as δ2/δ1 increases. The electrical angle of the zero-crossing point is calculated by Equations (11) and (12):

$$\alpha = \operatorname{arccot}\left[k \csc \theta_{cp} + \cot \theta_{cp}\right] \tag{11}$$

$$k = \frac{\delta_{PM(i+1)}}{\delta_{PMi}} \tag{12}$$

As we can see in Equations (10) and (11), the electrical angle of the zero-crossing point is determined by two adjacent faulty PMs. It means that it must have a zero-crossing point when two consecutive PMs are demagnetized. Similarly, we analyze varying demagnetization severities of the permanent magnets in S6; the normalized residual voltage waveforms are shown in Figure 7.

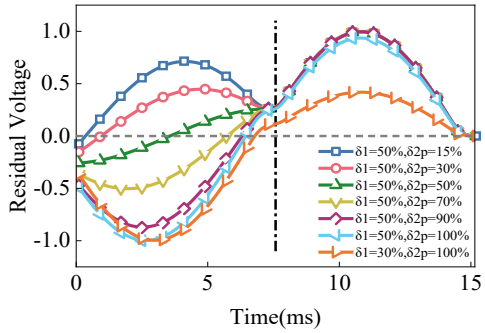


Figure 7. The normalized residual voltage waveforms under different demagnetized severities of PMs in S6.

As shown in Figure 7, when PM1 and PM2p are demagnetized, there is a zero-crossing point in Part 2 which moves to the electrical cycle reference point as δ1/δ44 increases, which is consistent with Equations (11) and (12).

To further investigate the relationship between the defined signal average values and the demagnetization severity, the average values in the first and second half-cycles under each fault mode are extracted from Figures 6 and 7, and the results are listed in Tables 5 and 6. Based on extensive simulations and experiments, the threshold of the prototype is set to 0.06.

Table 5. The defined average values and the average values under different severities of demagnetization in S5.

Fault Mode	Fault Degree	V_{av}		$V_{d\text{-}av}$	
		Part I	Part II	Part I	Part II
F7 $\delta1 < \delta2$	$\delta1 = 0.5, \delta2 = 0.7$	0.64	−0.27	1	−1
	$\delta1 = 0.5, \delta2 = 0.9$	0.64	−0.52	1	−1
	$\delta1 = 0.5, \delta2 = 1.0$	0.60	−0.61	1	−1
	$\delta1 = 0.3, \delta2 = 1.0$	0.27	−0.62	1	−1
F8 $\delta1 = \delta2$	$\delta1 = 0.5, \delta2 = 0.5$	0.64	−0.02	1	0
F9 $\delta1 > \delta2$	$\delta1 = 0.5, \delta2 = 0.15$	0.64	0.41	1	1
	$\delta1 = 0.5, \delta2 = 0.3$	0.64	0.23	1	1

Table 6. The defined average values and the average values under different severities of demagnetization in S6.

Fault Mode	Fault Degree	V_{av}		$V_{d\text{-}av}$	
		Part I	Part II	Part I	Part II
F10 $\delta2p < \delta1$	$\delta1 = 0.5, \delta2p = 0.15$	0.45	0.60	1	1
	$\delta1 = 0.5, \delta2p = 0.3$	0.26	0.60	1	1
F11 $\delta1 = \delta2p$	$\delta1 = 0.5, \delta2p = 0.5$	0.01	0.60	0	1
	$\delta1 = 0.5, \delta2p = 0.7$	−0.24	0.60	−1	1
F12 $\delta2p > \delta1$	$\delta1 = 0.5, \delta2p = 0.9$	−0.49	0.60	−1	1
	$\delta1 = 0.5, \delta2p = 1.0$	−0.58	0.56	−1	1
	$\delta1 = 0.3, \delta2p = 1.0$	−0.61	0.25	−1	1

As shown in Tables 5 and 6, $V_{d\text{-}av}$ is the same under different fault severities through setting a reasonable threshold. Though the true average values of each part are influenced by k, the utilization of the defined average value can eliminate the changes in the average values of the same fault mode.

In summary, four feature vectors, consisting of the defined signal average value ($V_{d\text{-}av}$) in the first and second half-cycles and the zero-crossing point number (Z_C) of the waveform, can effectively distinguish the eight fault states and achieve precise localization of the demagnetization fault.

3.4. Diagnostic Process of Fault Diagnosis

The demagnetization fault diagnosis procedure is illustrated in the flowchart shown in Figure 8, and the specific diagnostic steps are as follows:

(1) Data processing: Firstly, the induced voltage of the SC is obtained by VAS. Then, the residual voltage is calculated. Finally, the residual voltage is divided into different modules depending on the length of the electrical period, and the normalization process is completed by Equation (7).

(2) Fault location: Firstly, the modules are divided into two parts by the electrical cycle mainline, and the four fault indicators are extracted from each part. Secondly, the state combination can be identified through the mapping relationships established in Table 3.

Then, the locations of faulty PMs can be determined according to the mapping relationship in Table 1. Finally, if k is more than the electrical period number, the states of all PMs in the motor are identified, and the locations of faulty PMs are confirmed.

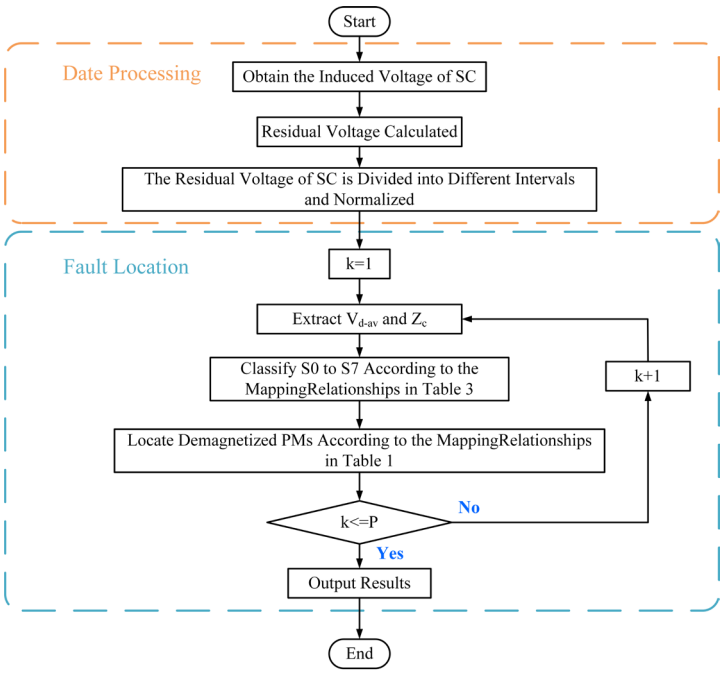


Figure 8. Flow chart of demagnetization localization method.

4. Simulation and Experimental Results

4.1. Simulation Results

In order to verify the robustness and effectiveness of the proposed demagnetization fault localization method, a three-phase PMSM with 48 slots and 44 poles is used. The key parameters of the motor are summarized in Table 7.

Table 7. The key parameters of the test PMSM.

Items	Values	Unit
Stator out diameter	270	mm
Stator inner diameter	203	mm
Air-gap length	1.0	mm
Winding wire diameter	1	mm
Thickness of PM	4.5	mm
Pole arc coefficient	0.73	/
Axial length	100	mm
Rated power	1.5	kW
Rated speed	180	rpm
Rated current	4	Arms
Number of phases	3	/
Number of coils	24	/
Coil turns	70	/
Parallel circuits per phase	1	/
Slot–pole combination	48–44	/

The finite element method (FEM) is used to simulate the demagnetization faults under different fault modes and operating conditions. Table 8 shows the different preset fault modes, and four fault indicators are extracted from the simulation results.

Table 8. Simulation fault settings and two localization indicators.

Preset Fault Mode	Operate Conditions	Electrical Period Number	Part I		Part II	
			Z_c	$V_{d\text{-}av}$	Z_c	$V_{d\text{-}av}$
S6-F11 δ34 = δ35 = 0.5	(a) 180r/min, rated load (b) 180r/min, half-rated load (c) 90r/min, rated load (d) 90r/min, half- rated load	17th	0	0	0	−1
		18th	1	0	0	1
S7(c)-F24 δ6 (0.5) = δ7 (0.5) > δ8 (0.3)	180r/min, rated load	3rd	0	0	0	−1
		4th	1	0	1	1
		5th	0	−1	0	0

The simulation results of the SC residual voltage are shown in Figure 9.

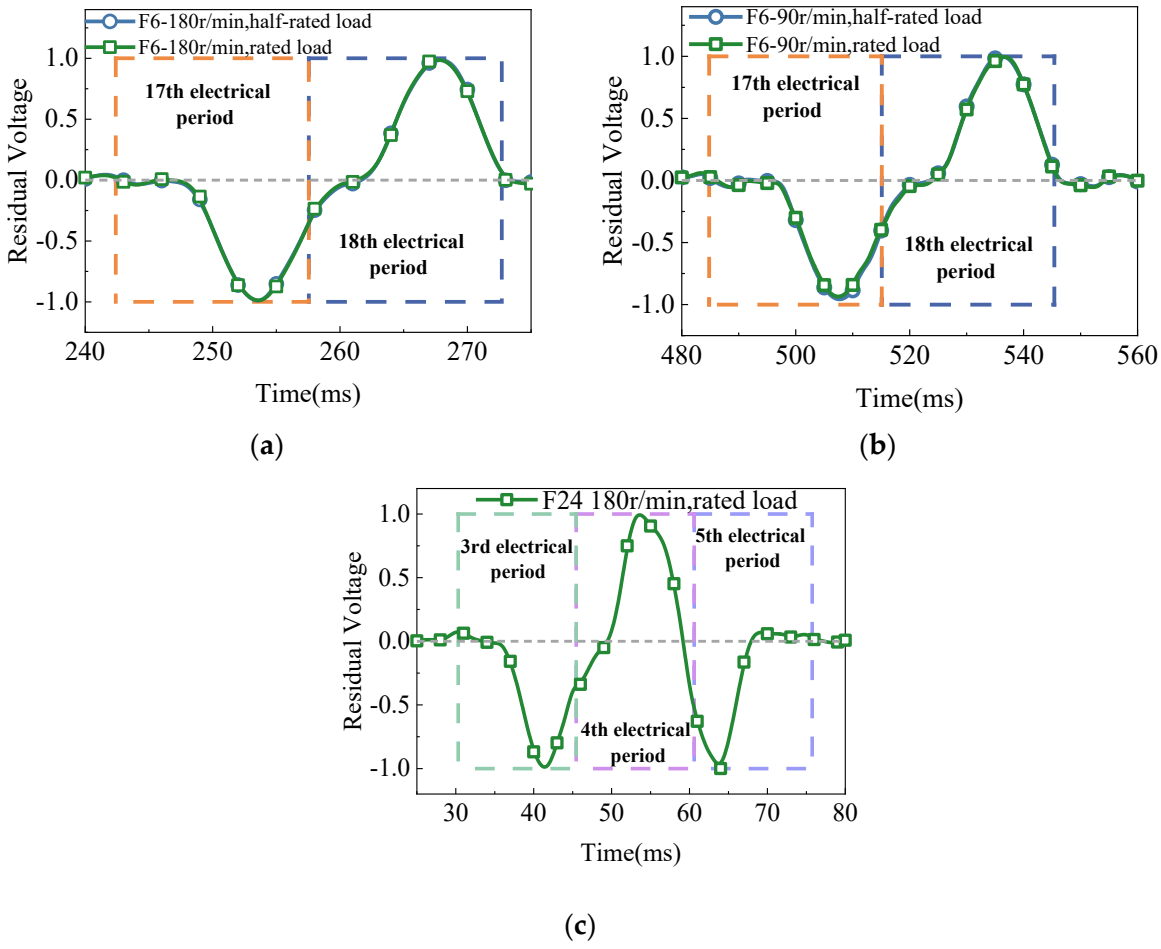


Figure 9. Simulation results of the SC residual voltage. (**a**) F6-180r/min; (**b**) F6-90r/min; (**c**) F24.

As shown in Figure 9a,b, the SC residual voltage of fault mode S6-F11 remains identical under four different operating conditions. The faulty PMs can be located according to the proposed diagnostic process in Figure 8. According to the mapping relationship in Table 1, the residual voltage located in the 17th electrical period is affected by the states of PM32, PM33, and PM34. The fault indicators are extracted from two parts of the residual voltage. By comparing the mapping relationships in Table 3, it can be concluded that PM32 and PM33 are healthy, and PM34 is faulty, which is consistent with the preset fault modes; thus, the effectiveness of the proposed demagnetization fault diagnosis method is validated. Similarly, the residual voltage locating in the 18th electrical period is affected by the states

of PM34, PM35, and PM36. It can also be concluded that PM34 and PM35 are faulty, and PM36 is healthy. The residual voltages locating in the other electrical periods are almost zero; therefore, the faulty PMs are PM34 and PM35, which is consistent with the preset fault modes. Although the operating conditions are different, the diagnosis results are the same. Therefore, the fault localization indicators are robust to different loads and speeds.

As we can see in Figure 9c, the faulty PMs can be located by sequentially detecting residual voltage waveforms during the third, fourth, and fifth electrical periods. This is not described in detail here. The simulation results are the same as the preset faulty PMs, which verifies the effectiveness of the method.

To further validate the effectiveness and generality of the method proposed in this paper, several prototypes with different pole and slot counts, topological structures, and winding configurations were used, as shown in Table 9.

Table 9. Three configurations of PMSM.

Motor Type Number	Slots/Poles	Layer	Pitch	Rotor Topology
Prototype 1	72/66	Double	Fractional	Surface-mounted magnet
Prototype 2	48/8	Single	Full	Interior magnet

It should be noted that the proposed diagnostic principle is fundamentally independent of the specific slot–pole combination and rests instead on three invariant relationships. First, the rotor PMs are partitioned into p modules, where p is the number of pole pairs, with each module containing three PMs as a geometric consequence of the alternating N–S magnetic pole arrangement. Second, feature extraction is performed over one electrical period, which corresponds to $1/p$ of a mechanical revolution—a universal timescale for all PMSM designs regardless of slot count. Third, the eight state combinations (S0–S7) and the 26 fault patterns (F0–F25) are derived solely from the relative demagnetization severity among the three PMs within a module. These relationships hold for any PMSM, making the proposed method scalable to different motor designs.

As shown in Table A1, 60 finite element simulation experiments were conducted on three prototypes, covering various rotational speeds, loads, fault severities, and fault types. The results indicate that the proposed method can accurately identify fault modes and locate demagnetized permanent magnets across different motors and operating conditions, achieving 100% diagnostic accuracy, fully validating its effectiveness and universality.

Since finite element simulations do not account for environmental noise during actual operation, this paper superimposed Gaussian white noise with signal-to-noise ratios of 5 dB, 15 dB, 20 dB, 25 dB, and 30 dB on each failure mode listed in Table A1, yielding a total of 300 sets of noisy test data. Statistical analysis of the failure diagnosis results for the above data indicates that 294 diagnoses were correct, with only six misdiagnoses. The overall diagnostic accuracy reached 98%, with a standard deviation of 0.81% and a 95% confidence interval of [96.4%, 99.6%]. Furthermore, the diagnostic thresholds established in this study provide ample margin to account for measurement uncertainties that may arise during actual operation. These results fully validate the robustness and effectiveness of the proposed method under high-noise and measurement uncertainty conditions.

4.2. Experimental Results

Figures 10 and 11 show the components of the experimental platform and the experimental prototype, respectively.

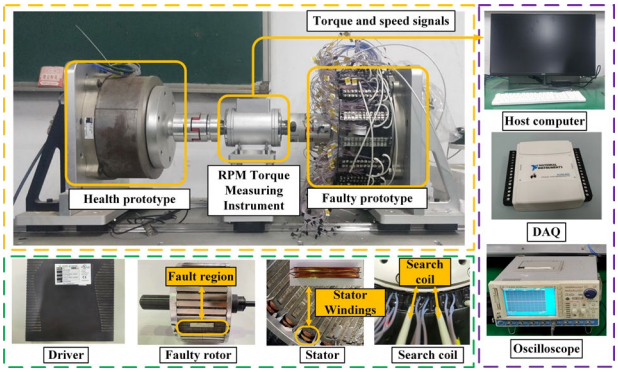


Figure 10. Experimental platform.

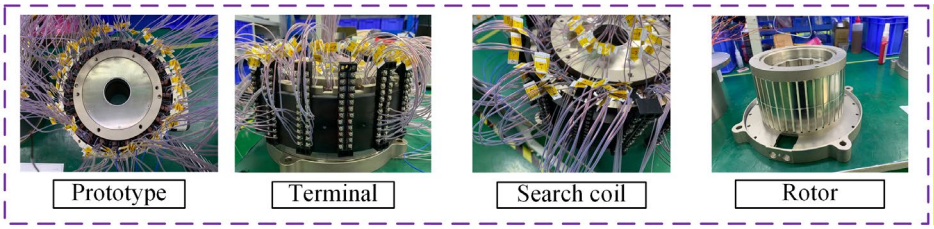


Figure 11. Experimental prototype.

Figure 10 shows the experimental platform which is composed of a healthy prototype (Yokokawa DMF280-270FE, Shenzhen, China), a faulty prototype (Yokokawa DMF280-270FE Shenzhen, China), a driver (Yokokawa VCII-10-230, Shenzhen, China), a host computer, a torque transducer (ZhonghangKedian ZH07-AZ, Beijing, China), an oscilloscope, and a data acquisition card (NI USB-6009, Suzhou, China) with 48 KS/s sampling rate and 12-bit ADC resolutions.

The method for accurately obtaining the real-time induced voltage of the SC is important for fault diagnosis. To obtain the induced voltage of the SC, the voltage acquisition system (VAS) is adopted which is composed of a data acquisition card (DAQ) and a host computer. Figure 12 shows the schematic diagram of the signal acquisition schematic and Table 10 shows the key parameters of DAQ.

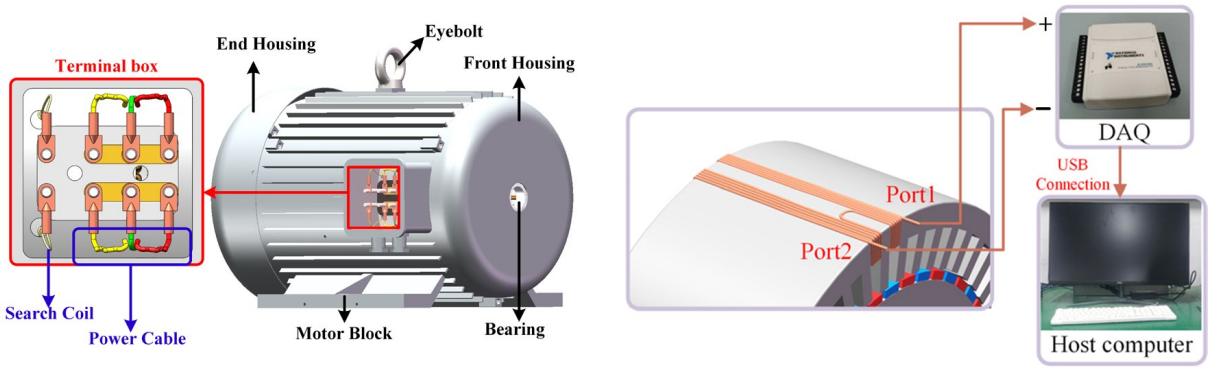


Figure 12. Voltage acquisition system schematic: (**a**) schematic diagram of the search coil lead connection; (**b**) schematic diagram of the VAS connection.

The two ports of the SC, as shown in Figure 12a, are led out by pre-milled slots in the motor terminal box first. Then, one port is connected to the analog input of the DAQ, and the other port is connected to the ground, as shown in Figure 12b. The real-time induced voltage is transmitted to the host computer through the USB connection. As the external

circuit resistance is much greater than the resistance of the SC, the current flowing through the SC is almost zero, which has a minimal effect on the performance of the motor.

Table 10. The key parameters of the data acquisition card.

Key Parameter	Value
Resolution	16 bits
Maximum sample rate	250 kS/s
Channel	8 RSE/4 NRSE
Range	±10 V, ±5 V, 0~10 V, 0~5 V
Program-controlled gain	1, 2, 4, 8 times
Calibration method	Software automatic calibration
Bus type	USB 2.0 high speed
Operating system	XP, Win7, Win8, Win10

In order to simulate the demagnetized fault of PMs, we divide each PM in the motor into two subunits. Removing one of the subunits simulates a 50% demagnetization fault, and removing both subunits simulates a 100% demagnetization fault. Due to the high cost of prototype manufacturing and the fact that each physical prototype can only implement a single fixed demagnetization mode, and given the current limitations of our laboratory resources, we were only able to construct a single fault mode. Therefore, experimental validation was conducted for only one fault mode. The experimental result is shown in Figure 13.

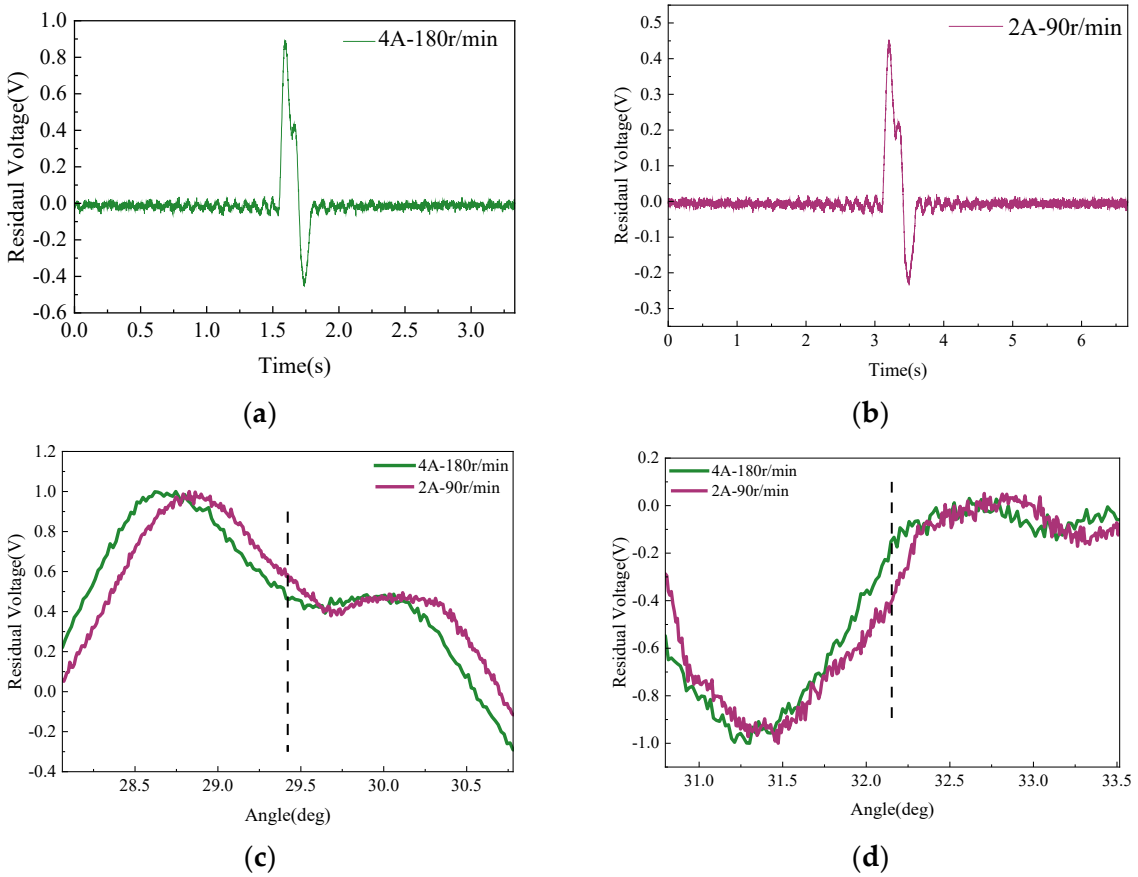


Figure 13. Experimental result of the SC residual voltage. (**a**) residual voltage under 4A-180r/min condition; (**b**) residual voltage under 2A-90r/min condition; (**c**) residual voltage-angle curve under different conditions; (**d**) residual voltage-angle curve under different conditions.

As shown in Figure 13a,b, the residual voltage under different operating conditions exhibits the same trend of variation. The signal is partitioned using modularization, and the residual voltages of the 11th and 12th electrical cycles are normalized, as illustrated in Figures 13c and 13d, respectively. The fault characteristics for the two electrical cycles are [0,1,1,1] and [0,−1,0,0], corresponding to the magnetic state combinations S5 and S1. This indicates that two permanent magnets experienced demagnetization faults during the 11th electrical cycle. The experimental results demonstrate the effectiveness and accuracy of the proposed feature analysis and diagnostic method.

4.3. Comparison with Other Methods

To further demonstrate the superiority and engineering practicality of the method proposed in this paper, we compare it with three mainstream demagnetization fault diagnosis methods. The detailed comparison results are shown in Table 11.

Table 11. Comparison of different methods for diagnosing demagnetization faults.

References	Methods	Fault Types Detected	Fault Localization	Computational Complexity	Hardware Cost	Invasiveness
[6,7]	MCSA-based method	Local demagnetization	No	Low	Low	None
[10,11]	ZSVC-based method	Local demagnetization	No	Low	Low	Low
[8]	Machine learning techniques-based method	Local demagnetization	No	High	Medium	None
Proposed method	Search coil-based method	Local demagnetization and uniform demagnetization	Yes	Low	Low	Low

As shown in Table 11, compared with methods based on MCSA, ZSVC analysis, and ML techniques, the method proposed in this paper is the only one capable of both detecting uniform demagnetization faults and accurately locating the demagnetized permanent magnet, while maintaining low computational complexity and hardware cost. Therefore, the method proposed in this paper offers significant advantages for diagnosing demagnetization faults in PMSMs.

From an engineering implementation perspective, the proposed two toroidal-yoke search coil configuration, although invasive to some extent, demonstrates high practicality. Each search coil is wound with only five turns of 0.5 mm copper wire, and its impact on normal motor operation is negligible, with extremely low cost. The search coils are wound around the stator yoke through the slot region, and the lead wires can be routed out via small pre-milled channels in the terminal box, requiring no modification to the main winding insulation or the mechanical air gap, thereby substantially reducing installation complexity and material cost. Consequently, this scheme can either be embedded during the motor manufacturing stage at almost no additional cost or be retrofitted into existing motors where conditions permit. For motors already in service, the feasibility of retrofitting depends primarily on the stator slot geometry and winding encapsulation method. Motors with open-slot or semi-open-slot designs are relatively easy to retrofit: After removing the end cover, the pre-formed toroidal coils can be directly inserted into the stator yoke slot clearances without dismantling the original stator windings. In contrast, retrofitting motors with fully potted or heavily impregnated windings is considerably more challenging and must be evaluated on a case-by-case basis according to the specific operating conditions.

5. Conclusions

This paper has proposed a minimally invasive demagnetization fault diagnosis method for permanent magnet synchronous motors, enabling precise localization of demagnetized PMs under arbitrary demagnetization patterns. Simulations and experimental results justify the effectiveness and robustness of the proposed method.

(1) Unlike conventional approaches that require a large number of intrusive search coils, the proposed method employs only two toroidal-yoke search coils installed in the stator slots. This configuration significantly reduces invasiveness while maintaining high diagnostic capability.

(2) In this paper, the rotor permanent magnets are divided into several modules, and based on the relative demagnetization levels of the magnets within each module, the infinite demagnetization patterns arising from continuous demagnetization severity are transformed into 26 representative patterns for analysis. By sequentially diagnosing the states of the permanent magnets in each module, precise localization of demagnetization faults is achieved, effectively resolving the combinatorial explosion problem in multi-magnet permanent magnet motors. This method is particularly well suited for PMSMs with multi-pole-pair configurations.

(3) The proposed method enables precise localization of demagnetization faults under arbitrary fault patterns. Among these, the uniform demagnetization fault corresponds to Fault Mode F14 in Table 2, demonstrating that the method is uniformly applicable to the diagnosis of both uniform and local demagnetization, while also achieving accurate location identification in the case of local demagnetization. These results provide critical information for the formulation of post-fault operation strategies and maintenance decisions.

(4) Theoretical analysis and experimental results demonstrate that the residual voltage waveforms over a single electrical period exhibit significant and stable differences across the eight fault states. By extracting feature vectors consisting of the defined average voltages in the first and second half-cycles and the zero-crossing points number, the proposed method achieves accurate differentiation of the eight fault states without the need for complex feature extraction, pattern recognition algorithms, or machine learning models.

Although the method is invasive, it does not affect the performance of the motor, and it can locate faulty PMs while imposing a low computational burden.

Author Contributions: Conceptualization, C.G.; supervision, C.G.; writing—review and editing, C.G. and Z.S.; writing—original draft, Z.S.; visualization, Z.S.; software, Z.S.; data curation, Z.S. project administration, J.D., X.X. and J.S. All authors have read and agreed to the published version of the manuscript.

Funding: This work was supported by the National Natural Science Foundation of China (Grant No. 52177039), the Natural Science Foundation of Henan Province (Grant No. 252300421328), and the Fundamental Research Funds for the Universities of Henan Province (Grant No. NSFRF240306).

Data Availability Statement: The data that support the findings are available from the corresponding author upon reasonable request.

Conflicts of Interest: The authors declare no conflicts of interest.

Appendix A

Table A1. Finite element simulation test results.

#	Motor Type	Speed (rpm)	Current (Arms)	Demagnetized Severity	Identified Fault Mode	Location Results	T/F
1	48-44	90	4	$\delta 6 = 0.6$, $\delta 8 = 0.3$	F6	PM6, PM8	T
2	48-44	225	4	$\delta 10 = 0.3$, $\delta 12 = 0.8$	F4	PM10, PM12	T
3	48-44	135	6	$\delta 11 = 0.2$, $\delta 12 = 0.8$	F7	PM11, PM12	T
4	48-44	225	6	$\delta 14 = 0.4$, $\delta 15 = 0.5$	F10	PM14, PM15	T
5	48-44	180	2	$\delta 18 = 0.4$, $\delta 19 = 0.5$, $\delta 20 = 0.5$	F19	P18, PM19, PM20	T
6	48-44	135	2	$\delta 18 = 0.4$, $\delta 19 = 0.5$, $\delta 20 = 0.7$	F18	PM18, PM19, PM20	T
⋮	⋮	⋮	⋮	⋮	⋮	⋮	T
21	72-66	200	28	$\delta 24 = 0.5$, $\delta 25 = 0.3$	F12	PM24, PM25	T
22	72-66	100	28	$\delta 25 = 0.3$, $\delta 26 = 0.8$	F7	PM25, PM26	T
23	72-66	150	14	$\delta 28 = 0.7$, $\delta 29 = 0.2$	F12	PM28, PM29	T
24	72-66	100	14	$\delta 32 = 0.4$, $\delta 33 = 0.6$, $\delta 34 = 0.7$	F23	PM32, PM33, PM34	T
25	72-66	225	36	$\delta 32 = 0.2$, $\delta 33 = 0.5$, $\delta 34 = 0.7$	F18	PM32, PM33, PM34	T
26	72-66	175	36	$\delta 32 = 0.4$, $\delta 33 = 0.5$, $\delta 34 = 0.2$	F25	PM32, PM33, PM34	T
⋮	⋮	⋮	⋮	⋮	⋮	⋮	T
55	48-8	2500	7	$\delta 4 = 0.2$, $\delta 5 = 0.3$, $\delta 6 = 0.4$	F23	PM4, PM5, PM6	T
56	48-8	2000	7	$\delta 4 = 0.2$, $\delta 5 = 0.7$, $\delta 6 = 0.3$	F20	PM4, PM5, PM6	T
57	48-8	3000	4	$\delta 4 = 0.2$, $\delta 5 = 0.3$, $\delta 6 = 0.5$	F18	PM4, PM5, PM6	T
58	48-8	2500	4	$\delta 4 = 0.2$, $\delta 5 = 0.2$, $\delta 6 = 0.5$	F22	PM4, PM5, PM6	T
59	48-8	3000	9	$\delta 4 = 0.2$, $\delta 5 = 0.3$, $\delta 6 = 0.3$	F19	PM4, PM5, PM6	T
60	48-8	2500	9	$\delta 4 = 0.2$, $\delta 5 = 0.15$, $\delta 6 = 0.3$	F16	PM4, PM5, PM6	T

References

1. Yu, Y.; Chai, F.; Pei, Y.; Doppelbauer, M.; Lee, C.H.T. Comparative Study of Loss Characteristic Between Permanent Magnet Synchronous Machine and Vernier Machine for In-Wheel Direct Drive. *IEEE Trans. Transp. Electrif.* **2025**, *11*, 2035–2048. [CrossRef]
2. Han, S.; Zhang, Y.; Xiao, X.; Guo, Q. Adaptive Harmonic Elimination Model Predictive Current Control of PMSM in Aviation Electric Propulsion Systems. *IEEE J. Emerg. Sel. Top. Power Electron.* **2025**, *13*, 4445–4458. [CrossRef]
3. Gao, C.; Gao, B.; Xu, X.; Si, J.; Hu, Y. Automatic Demagnetization Fault Location of Direct-Drive Permanent Magnet Synchronous Motor Using Knowledge Graph. *IEEE Trans. Instrum. Meas.* **2024**, *73*, 3502312. [CrossRef]
4. Zhong, Q.; Mao, K.; Wang, K.; Le, Y.; Zheng, S. Demagnetization Fault Diagnosis for Magnetically Suspended PMSM Using Rotor Displacement Signals. *IEEE Trans. Instrum. Meas.* **2023**, *72*, 3518012. [CrossRef]
5. Cheng, M.; Hang, J.; Zhang, J. Overview of fault diagnosis theory and method for permanent magnet machine. *Chin. J. Electr. Eng.* **2015**, *1*, 21–36. [CrossRef]
6. Haddad, R.Z.; Strangas, E.G. On the Accuracy of Fault Detection and Separation in Permanent Magnet Synchronous Machines Using MCSA/MVSA and LDA. *IEEE Trans. Energy Convers.* **2016**, *31*, 924–934. [CrossRef]
7. Riba Ruiz, J.-R.; Rosero, J.A.; Garcia Espinosa, A.; Romeral, L. Detection of Demagnetization Faults in Permanent-Magnet Synchronous Motors Under Nonstationary Conditions. *IEEE Trans. Magn.* **2009**, *45*, 2961–2969. [CrossRef]
8. Kao, I.-H.; Wang, W.-J.; Lai, Y.-H.; Perng, J.-W. Analysis of Permanent Magnet Synchronous Motor Fault Diagnosis Based on Learning. *IEEE Trans. Instrum. Meas.* **2019**, *68*, 310–324. [CrossRef]

9. Skowron, M.; Orlowska-Kowalska, T.; Kowalski, C.T. Diagnosis of Stator Winding and Permanent Magnet Faults of PMSM Drive Using Shallow Neural Networks. *Electronics* **2023**, *12*, 1068. [CrossRef]
10. Urresty, J.-C.; Riba, J.-R.; Romeral, L. Influence of the Stator Windings Configuration in the Currents and Zero-Sequence Voltage Harmonics in Permanent Magnet Synchronous Motors with Demagnetization Faults. *IEEE Trans. Magn.* **2013**, *49*, 4885–4893. [CrossRef]
11. Urresty, J.-C.; Riba, J.-R.; Delgado, M.; Romeral, L. Detection of Demagnetization Faults in Surface-Mounted Permanent Magnet Synchronous Motors by Means of the Zero-Sequence Voltage Component. *IEEE Trans. Energy Convers.* **2012**, *27*, 42–51. [CrossRef]
12. Ebrahimi, B.M.; Faiz, J. Demagnetization Fault Diagnosis in Surface Mounted Permanent Magnet Synchronous Motors. *IEEE Trans. Magn.* **2013**, *49*, 1185–1192. [CrossRef]
13. Alameh, K.; Cité, N.; Hoblos, G.; Barakat, G. Vibration-based fault diagnosis approach for permanent magnet synchronous motors. *IFAC-PapersOnLine* **2015**, *48*, 1444–1450. [CrossRef]
14. Xing, M.; Ding, H.; Ren, X.; Wang, T.; Ge, S.; Shen, J. On the Accuracy of Rotor Demagnetization Fault Detection in PMSM Using Vibration-Based Condition Indicators. In Proceedings of the 2021 CAA Symposium on Fault Detection, Supervision, and Safety for Technical Processes (SAFEPROCESS), Chengdu, China, 17–18 December 2021; pp. 1–6. [CrossRef]
15. Huang, F.; Zhang, X.; Qin, G.; Xie, J.; Peng, J.; Huang, S.; Tang, Y. Demagnetization Fault Diagnosis of Permanent Magnet Synchronous Motors Using Magnetic Leakage Signals. *IEEE Trans. Ind. Inform.* **2023**, *19*, 6105–6116. [CrossRef]
16. Goktas, T.; Zafarani, M.; Lee, K.W.; Akin, B.; Sculley, T. Comprehensive Analysis of Magnet Defect Fault Monitoring Through Leakage Flux. *IEEE Trans. Magn.* **2017**, *53*, 8201010. [CrossRef]
17. Song, J.; Zhao, J.; Dong, F.; Zhao, J.; Xu, L.; Yao, Z. A New Demagnetization Fault Recognition and Classification Method for DPMSLM. *IEEE Trans. Ind. Inform.* **2020**, *16*, 1559–1570. [CrossRef]
18. Mohammed, A.; Melecio, J.I.; Djurović, S. Electrical Machine Permanent Magnets Health Monitoring and Diagnosis Using an Air-Gap Magnetic Sensor. *IEEE Sens. J.* **2020**, *20*, 5251–5259. [CrossRef]
19. Da, Y.; Shi, X.; Krishnamurthy, M. A new approach to fault diagnostics for permanent magnet synchronous machines using electromagnetic signature analysis. *IEEE Trans. Power Electron.* **2013**, *28*, 4104–4112. [CrossRef]
20. Zeng, C.; Huang, S.; Lei, J.; Wan, Z.; Yang, Y. Online rotor fault diagnosis of permanent magnet synchronous motors based on stator tooth flux. *IEEE Trans. Ind. Appl.* **2021**, *57*, 2366–2377. [CrossRef]
21. Im, J.-H.; Kang, J.-K.; Hur, J. Static and Dynamic Eccentricity Faults Diagnosis in PM Synchronous Motor Using Planar Search Coil. *IEEE Trans. Ind. Electron.* **2023**, *70*, 9291–9300. [CrossRef]
22. Rafaq, M.S.; Lee, H.J.; Park, Y.; Lee, S.B.; Zapico, M.O.; Fernandez, D.; Reigosa, D.; Briz, F. Airgap search coil based identification of PM synchronous motor defects. *IEEE Trans. Ind. Electron.* **2022**, *69*, 6551–6560. [CrossRef]
23. Chen, H.; Gao, C.; Si, J.; Nie, Y.; Hu, Y. A novel method for diagnosing demagnetization fault in PMSM using toroidal-yoke-type search coil. *IEEE Trans. Instrum. Meas.* **2021**, *71*, 7501012. [CrossRef]
24. Gao, C.; Li, B.; Chen, H.; Xu, Y.; Xu, X.; Si, J.; Hu, Y. A Less-Invasive Method for Accurately Diagnosing Demagnetization Fault in PMSM Using Rotor Partition. *IEEE Trans. Transp. Electrif.* **2023**, *9*, 2356–2366. [CrossRef]
25. Tang, S.; Cao, Y.; Shi, T.; Yan, Y.; Xia, C. Online Estimation of Load Torque and Moment of Inertia Incorporating Extended Disturbance Observer With Trigger. *IEEE Trans. Power Electron.* **2025**, *40*, 5731–5742. [CrossRef]
26. Yang, C.; Liu, W.; Niu, S.; Lyu, J.; Chau, K.T. Parameter-Tuning-Free Two-Step Identification of Mechanical Parameters for PMSM Drives. *IEEE Trans. Ind. Electron.* **2025**, *72*, 12378–12392. [CrossRef]

Disclaimer/Publisher's Note: The statements, opinions and data contained in all publications are solely those of the individual author(s) and contributor(s) and not of MDPI and/or the editor(s). MDPI and/or the editor(s) disclaim responsibility for any injury to people or property resulting from any ideas, methods, instructions or products referred to in the content.